43rd Aerospace Sciences Meeting and Exhibit, Jan.10-13 2005, Reno, NV

Towards Large Eddy Simulation of Film-Cooling Flows on a Model Turbine Blade Leading Edge

Ioulia V. Iourokina* and Sanjiva K. Lele†

Stanford University, Stanford, CA, 94305

Film cooling is used in turbine engines to avoid the critical heat loads on blade surfaces. The flowfield resulting from hot and cold gas interaction is rather complex and film-cooling effectiveness can be significantly reduced if intensive mixing occurs. The purpose of the present study is to investigate this interaction numerically, using Large Eddy Simulation. Special computational procedure coupling two different numerical codes is developed in order to tackle this problem. The performance of the coupling procedure is tested on steady and unsteady laminar flow problems. This methodology is then applied to the calculations of a jet in a crossflow as a model problem representing the flow interactions occurring during film-cooling.

I. Introduction

The overall performance of the gas turbine engine increases with the turbine inlet temperature. In modern turbines the hot gas temperature exceeds the melting point of the blade material. Film cooling, along with other cooling mechanisms (impingement cooling, rib/pin augmented cooling etc.), is used in turbine engines to alleviate the turbine blade heat loads. Since the cool air for film cooling is drawn from the compressor, blade cooling implies an aerodynamic penalty. The complex mechanism of turbulent mixing between hot and cold gases makes it challenging to design film cooling schemes which give good and reliable cooling performance and minimize losses. Computational investigation of this problem can shed some light onto the film cooling physics, thus helping designers in choosing the optimum configuration.

A number of experimental studies of this problem have been done in the past. Different geometries of the cooled surface were investigated, featuring flat plate,[1,2] cylinder,[3,4,5] gas turbine airfoil.[6,7,8,9] Among numerical investigations of film-cooling are the series of calculations by Leylek et al.,[10,11,12] simulations of Tyagi et al.,[13] who performed a detailed analysis of film-cooling flowfield above the flat plate. Some numerical studies of the airfoil film-cooling have also been done.[14,15]

Summarizing the results obtained by the previous investigators, we can identify several important features of the problem. First of all, the flow in the film hole is far from the fully developed Poiseuille flow, especially when realistic small L/d ratios are used. Moreover, as Leylek et al.[10] showed, under certain conditions the peak turbulence levels occur inside the film hole, thus making it the region of the dominant turbulence production. The behavior of the flow downstream of the jet exit is quite sensitive to the details of the flow inside the film hole. Also, strong coupling exists between the flow above the film-cooling surface and the flow in the film hole. Therefore, it is difficult to obtain a good performance by modeling the coolant inflow as a prescribed artificial boundary condition; the film hole and plenum geometry should be included in the simulations in order to accurately describe the phenomenon.

The vast majority of numerical simulations of film-cooling flows have been obtained using Reynolds-averaged Navier-Stokes equations with two-equation models for turbulence. However, complex anisotropic turbulent structures pertinent to this type of flows are not resolved with this approach (for example, see Ref. 13). Large Eddy Simulations, which compute the large-scale turbulent structures directly as opposed

---

[*] Research Assistant, Department of Aeronautics and Astronautics, AIAA Member

[†] Professor, Department of Aeronautics and Astronautics and Department of Mechanical Engineering, AIAA Member

to modeling them, is much more better for this problem. There are very few Large Eddy Simulations of film cooling flows, documented in the literature. Calculations of Tyagi et al.[13] is one recent study. The film-cooled surface in their investigations is a flat plate. Equations solved are the incompressible Navier-Stokes equations together with the scalar equation for temperature. Since in the real gas turbine engine the flow is in high-subsonic or transonic regime, the full compressible equations should generally be used for better approximation of the film-cooling environment.

To the authors knowledge, there are no detailed numerical investigations, such as Large Eddy Simulations or Direct Numerical Simulations, of film-cooling flows in the vicinity of the leading edge of a turbine blade. Such a simulation must represent the turbine blade with a compressible flow around it, film-holes carrying the coolant and the plenum with a slow moving flow. Due to the difference in geometry and flow regimes, numerical methods which are the most efficient for describing each of these components individually, are also different. Instead of trying to pick one numerical code which would work ”in average” for the whole problem, separate numerical codes for each individual component can be used. This way one can be sure that the best performance for each part of the problem is achieved, resulting in good overall performance, provided that efficient and accurate coupling procedure can be proposed.

In the present paper, such a ”composite” numerical method is developed. Numerical code solving compressible Navier-Stokes equations is utilized in the region above the cooled surface. The code allows for an arbitrary curvature of the blade surface, which enables investigations of film-cooling at the leading edge region of a model turbine blade. Low Mach number approximation is used for the flow inside the plenum and film holes. The coupling procedure used to join these codes together is described in this paper. The implementation of coupling procedure is extensively tested on laminar steady and unsteady problems. Finally, this method is applied to the calculations of jet in a crossflow as a model problem representing the flow interactions occurring during film-cooling.

II. Numerical method

The goal of performing Large Eddy Simulations of film-cooling in the leading edge region of a model turbine blade motivated the development of a special numerical procedure. Figure 1 shows the schematic of a model turbine blade with film-cooling holes in the vicinity of a leading edge. The film-cooling holes are fed by a plenum.

We can identify two different regions pertinent to this film-cooling configuration.

1. *Region exterior to the turbine blade surface* is shown as striped in Figure 1. The flow which impinges a turbine blade after leaving the combustor occupies this region. This flow is usually at a high-subsonic or transonic state and it carries free-stream turbulence with it. Compressibility effects are important in this region. Therefore, fully compressible Navier-Stokes equations are solved in the exterior region.

2. *Plenum and film holes* are shown in black in Figure 1. Mach number is rather small inside the supply plenum since the flow is practically stagnant there due to a large volume of plenum chamber. Use of compressible code without preconditioners in this region would result in severe time step limitations. Efficient preconditioners for the full Navier-Stokes equations continue to be a topic of research in various groups. Alternatively, low Mach number approximation can be employed. In the present study, plenum and film holes are treated numerically with a low Mach number variable density code.

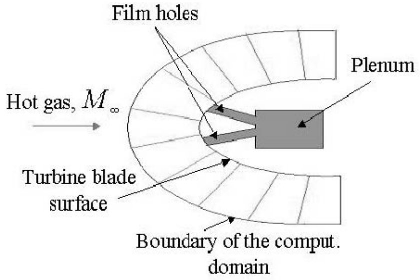

Figure 1. Schematic of a model turbine blade with film-holes.

Therefore, each of these two regions is calculated with its own numerical code. Special parallel interface is created for coupling these two codes together and providing an exchange of boundary conditions.

A. Compressible code

Compressible code which is used in the exterior region (striped region in Fig. 1) was developed by Z. Xiong.[16] Compressible Navier-Stokes equations in primitive variables are solved numerically using implicit time integration with an approximately-factorized difference scheme. The spatial discretization is achieved by mapping the body-fitted mesh coordinates from physical space (x, y, z) to the uniform computational space (ξ, η, z). Fourth-order accurate central-difference scheme is used for first - and second- derivatives in the computational space. Details of the numerical implementation of the compressible code can be found in Ref. 17.

B. Low Mach number code

Low Mach number code which is used in the plenum and film holes (black region in Fig. 1) is written by C. Pierce.[18] The set of equations solved numerically is the low Mach number approximation of the Navier-Stokes equations written in conservative form in cylindrical coordinates. Velocity components are staggered with respect to density and other scalars in both space and time.[19] Second order central difference scheme is used for the integration of momentum equations, while QUICK scheme[20] is employed for scalar advection to avoid the formation of spatial oscillations. Second-order Crank-Nikolson scheme with sub-iterations is used for time advancement. Advection and diffusion terms in radial and azimuthal directions are treated implicitly. Poisson equation for pressure is solved with the multigrid method. For more details, the reader is referred to Ref. 18.

Both codes are written in LES formulation with dynamic Smagorinsky eddy-viscosity model[21] used for the treatment of subgrid-scale terms.

C. Coupling the codes

Parallel interface for coupling the two codes is written on MPI platform. It constructs two disjoint groups of processes - one for each code. All communications within each group are performed using intracommunicators. Message passing between two groups is accomplished with the help of an intercommunicator. Time advancement of both codes is synchronized by choosing the global time step equal to the smallest among time steps of individual codes, as dictated by stability requirement: $\triangle\tau = \min(\triangle\tau_1, \triangle\tau_2)$. Exchange of variables across interfaces between computational domains of the two codes is performed at every time step. Details of implementation of this exchange are described in this section.

Computational domain

The upper half of the computational domain used in the calculations is shown at Figure 2. Compressible code domain corresponds to a region exterior to the turbine blade and shown as striped in Fig. 2. Low Mach number code domain corresponds to plenum and film hole in Fig. 2. Since the low Mach number code domain has to be cylindrical (the code is written in cylindrical coordinates) and surface of a model turbine blade is curved, there must be a region of overlap between two domains, which physically corresponds to the region above the turbine blade surface where cooling gas injection takes place. This region of overlap is calculated by both codes.

Only one boundary of the compressible code domain intersects the low Mach number code domain. This boundary is part of the turbine blade surface, and the intersection occurs at a place, where cooling gas is injected. Variables from the low Mach number code should be supplied to the compressible code at this location, which is schematically shown by the arrow 1 in Fig. 2. Boundaries of the low Mach number code domain which intersect the compressible code domain are shown in bold lines in Fig. 2. These are "free" boundaries of the low Mach number code domain, since they are not part of film hole walls. Variables from the compressible code should be supplied to the low Mach number code at these boundaries, which is schematically shown by arrows 2 in Fig. 2.

1. Variables supplied from the low Mach number code to the compressible code (referred as II C 1)

Variables, which are solved for in the compressible code, are $\{\rho, u, v, w, T\}$. All these variables should be specified at the location of cooling gas injection. Various ways of specifying these variables have been tested (the details of the test cases are described later in the paper). However, the best performance was achieved by interpolating all of the variables $\{\rho, u, v, w, T\}$ from the low Mach number code.

2. Variables supplied from the compressible code to the low Mach number code (referred as II C 2)

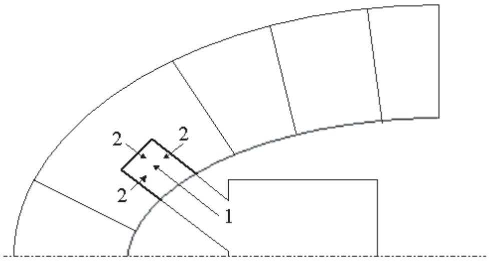

Figure 2. Upper part of a computational domain for calculation of film-cooling geometry.

In low Mach number code boundary conditions are required for the following variables. Momentum equations need values of three components of velocity $\{u, v, w\}$ at the boundaries. Scalar transport equation requires specification of a scalar (temperature) at the boundary. Density is obtained from temperature through the equation of state, therefore, no boundary conditions for density is required. $\{u, v, w, T\}$ are interpolated from compressible code at the "free" boundaries of low Mach number code domain (boundary surfaces of low Mach number code domain intersecting compressible code domain). The same procedure is applied regardless of whether the "free" boundary corresponds to an inflow or outflow.

In addition, we need boundary conditions for pressure for solving the Poisson equation. In the low Mach number approximation only the second order pressure $P^{(2)}(\vec{x}, t)$ enters the equations of motion (see, for example, Ref. 22). It is decoupled from density and temperature fluctuations and determined by the constraint on the divergence of velocity, much like the pressure in incompressible equations. Zeroth-order pressure $P^{(0)}(t)$ plays the role of the global thermodynamic pressure and enters the equation of state. Pressure field obtained in compressible equations is $P^{compr}(\vec{x}, t) = P^{(0)}(t) + P^{(2)}(\vec{x}, t)$. Taking gradient of P we have $\nabla P(\vec{x}, t) = \nabla P^{(2)}(\vec{x}, t)$.

In the present method, we solve the Poisson equation with Neumann boundary conditions for $P^{(2)}$. We specify the value of derivative $\frac{\partial P^{(2)}}{\partial \vec{n}}$ in the direction normal to the boundary surface. We interpolate $\frac{\partial P^{(2)}}{\partial \vec{n}} = \frac{\partial P^{compr}}{\partial \vec{n}}$ from the gradients of the compressible pressure field at the "free" boundaries of low Mach number code domain intersecting the compressible code domain. Zeroth-order pressure $P^{(0)}$ is then added to the calculated field of $P^{(2)}$ in order to set the right value of the total static pressure. We find the value of $P^{(0)}$ by matching $P^{compr} = P^{(0)} + P^{(2)}$ at one specific location in the region of overlap.

Other choices for specifying boundary conditions at the "free" boundaries of the low Mach number code domain are possible, for example, Dirichlet boundary conditions for the Poisson equation, normal derivatives for velocities instead of velocities itself. However, the method described above proved to work the best.

We use bilinear interpolation to interpolate values both from compressible to low Mach number code and from low Mach number to compressible code. Since the low Mach number code has a second-order accurate space discretization, increasing the order of interpolation beyond the second order does not lead to any further advantage, which was confirmed by numerical tests.

III. Testing the numerical method

There are two major questions which need to be addressed to check if the coupling procedure described above works satisfactorily.

1. Recall that there exists a region of overlap between the computational domains of the two codes (see Fig. 2). Since this overlap region is being computed by two different codes, it would be desirable for the convergence of the overall problem that individual solutions were close to each other in this region. The closeness of analytical solutions of compressible and low Mach number equations in the overlap region is provided by the fact that this region is contained within the turbine blade boundary layer, where the Mach number is small. However, it is necessary to check whether the numerical solutions are also close. So, the first part of the testing procedure investigates the closeness of solutions of individual codes in the regime of low Mach number.

2. The second part concerns the implementation of coupling procedure and behavior of the coupled

solution. Besides the closeness of solutions of individual codes one also needs to test the quality of the coupled solution. Convergence of the coupled solution to the solutions of individual codes as well as the accuracy of boundary condition exchange is investigated in the second part of the testing procedure.

A. Closeness of solutions of individual codes

The ability of two codes to individually reproduce similar results in the low Mach number regime was tested by placing the low Mach number code domain completely inside the compressible code domain in a low Mach number flow. One-way coupling was implemented. The low Mach number code obtained information from compressible code through all the boundaries by the method described in subsection II C 2. However, no information was transferred from the low Mach number code to the compressible code. Both steady and unsteady tests were performed in this setup.

1. Steady tests (referred as III A 1)

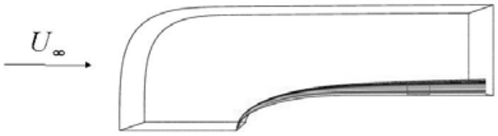

Figure 3. Computational domain for the steady test case. Temperature contours are shown.

Steady flow around a model turbine blade with uniform free-stream velocity U_∞ parallel to the flat portion of a blade surface was chosen as a steady test case. Schematic configuration of the computational domain is shown in Figure 3. The size of the compressible code domain is $(16D, 7.5D, 7D)$, where D is the diameter of the turbine blade leading edge. No-slip isothermal boundary conditions were employed everywhere at the turbine blade surface. For the test case shown, temperature at the wall was taken to be $T_w = 2T_{0\infty}$. Temperature contours along the plane perpendicular to the blade surface are also shown in Fig. 3 to show the size of the boundary layer. A cylindrical pipe with the diameter $0.5D$ and the height $0.5D$ was placed inside the compressible code domain. The bottom surface of the cylinder was located $0.01D$ above the turbine blade surface, thus making the cylinder fall well inside the boundary layer. The low Mach number code was used inside the cylindrical domain. Boundary conditions interpolated from compressible code as described in subsection II C 2 were specified at all boundaries of the low Mach number code domain. Flow parameters were $M_\infty = 0.05$ for the compressible code, $Re_D = \frac{U_\infty D}{\nu} = 1000$ for both codes.

Both codes were converged to the steady state and solutions obtained by the two codes were compared. Profiles of streamwise and vertical velocities, as well as temperature, taken through the point with maximum discrepancy, are shown in Fig. 4.

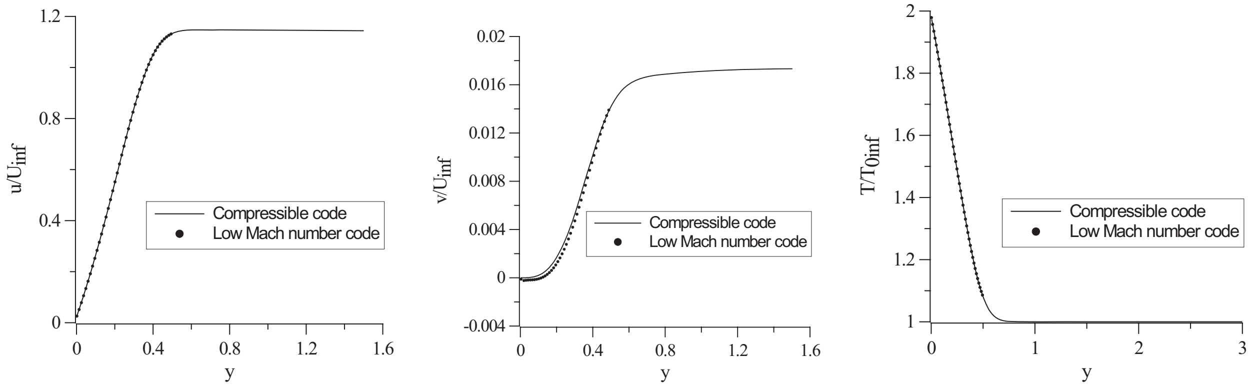

(a) Streamwise velocity.

(b) Vertical velocity.

(c) Temperature

Figure 4. Comparison of boundary layer profiles calculated with two codes.

It can be seen that the agreement between the two solutions is rather good.

2. Unsteady tests (referred as III A 2)

In order to check if unsteadiness influences the degree to which solutions differ from each other, the following unsteady test case was performed. Computational domain for the compressible code for this test case was the same as shown in Fig. 3. First, steady flow around the blade with uniform free-stream velocity was obtained. This is denoted as $\{\overline{\rho}, \bar{u}, \bar{v}, \bar{w}, \bar{T}\}$. Flow parameters were kept the same as in subsection III A 1 except that the turbine blade surface was colder: $T_w = 1.075T_{0\infty}$.

Velocity disturbance in the form of a circular Taylor vortex[23] was superimposed on the steady flow around the turbine blade:

$$v'_\phi = \frac{\mathcal{M}r}{16\pi\nu^2t^2}\exp(\frac{-r^2}{4\nu t});\ v'_r = v'_z = 0, \tag{1}$$

where v'_ϕ is tangential velocity, v'_r is radial velocity, v'_z is spanwise velocity and r is the distance from the center of the vortex.

Circular Taylor vortex is an analytical solution of unsteady viscous incompressible equations. Here $\mathcal{M} = \int_0^\infty 2\pi rvr\mathtt{d}r$ is an invariant of the flow.

Initial conditions for the present unsteady test case were set as

$$\begin{aligned} \rho &= \overline{\rho} \\ u &= \bar{u} + u' \\ v &= \bar{v} + v' \\ w &= 0 \\ T &= \bar{T}. \end{aligned}$$

Here u' and v' are disturbances from Eq. 1 written in cartesian coordinates. Parameters t and $\mathcal{M}$ of Eq. 1 were chosen to set initial radius of the vortex $R_T/D = 0.33$ (R_T is the distance from the vortex center to the point of maximum velocity) and initial velocity disturbance level $v'_{max}/U_\infty = 1\%$. The center of the vortex was located $4D$ above the blade surface and initially $4D$ upstream of the low Mach number code domain. The vortex was convected with the mean flow and captured by the low Mach number code as it passed through it.

Two-dimensional rectangular as well as three-dimensional cylindrical low Mach number code domains were investigated. Rectangular domain was of the size $(0.5D \times 1.5D)$, cylindrical domain had a radius $0.5D$ and a height $1.5D$. For rectangular configuration, two sets of tests were performed.

- Low Mach number code domain is perpendicular to the main stream. The lower boundary of the domain is located $1.5D$ higher than the turbine blade surface.
- Low Mach number code domain is inclined at 45° to the main stream. This test case was conducted in order to check whether the relative skewness of the grid lines of two codes influences the results.

For cylindrical configuration, the flow is two-dimensional, i.e. there is no variation of flow parameters in spanwise direction of the blade coordinate system. Typical snapshots of the vertical velocity v calculated with both codes are overlaid in Fig. 5 for perpendicular and inclined rectangular domains. The moment when the center of the vortex is in the low Mach number code domain is shown. It can be seen that the contours of vertical velocity of the two solutions are very close to each other. The same was observed for all other variables for both rectangular and cylindrical low Mach number code domains. Moreover, contours of vertical velocity show the largest difference.

Maximum difference between flow variables was calculated over the low Mach number code domain as

$$\Delta u_i = \frac{\max\left|u_i^{compr} - u_i^{lowMach}\right|}{U_\infty} \tag{2}$$

for velocity components and

$$\Delta P = \frac{\max\left|P^{compr} - P^{lowMach}\right|}{\rho_\infty U_\infty^2} \tag{3}$$

for pressure.

(a) Perpendicular domain.

(b) Inclined domain.

Figure 5. Vertical velocity contours for the convecting Taylor vortex.

The difference in velocity is plotted versus computational time in Fig. 6 for rectangular and cylindrical domains. The difference is larger when the center of the vortex is inside the low Mach number code domain. From Fig. 6(a) we see that orientation of the domain does not influence the maximum difference between solutions.

The difference in pressure, when properly normalized (Eq. 3), is about two orders of magnitude smaller than difference in velocity and is therefore not plotted here. It is consistent with the fact that the pressure gradient for the Taylor vortex satisfies

$$\partial p'/\partial r = \rho v'^2/r. \tag{4}$$

It is seen that pressure disturbance is of second order compared to velocity disturbance, which explains the smaller value of the pressure difference.

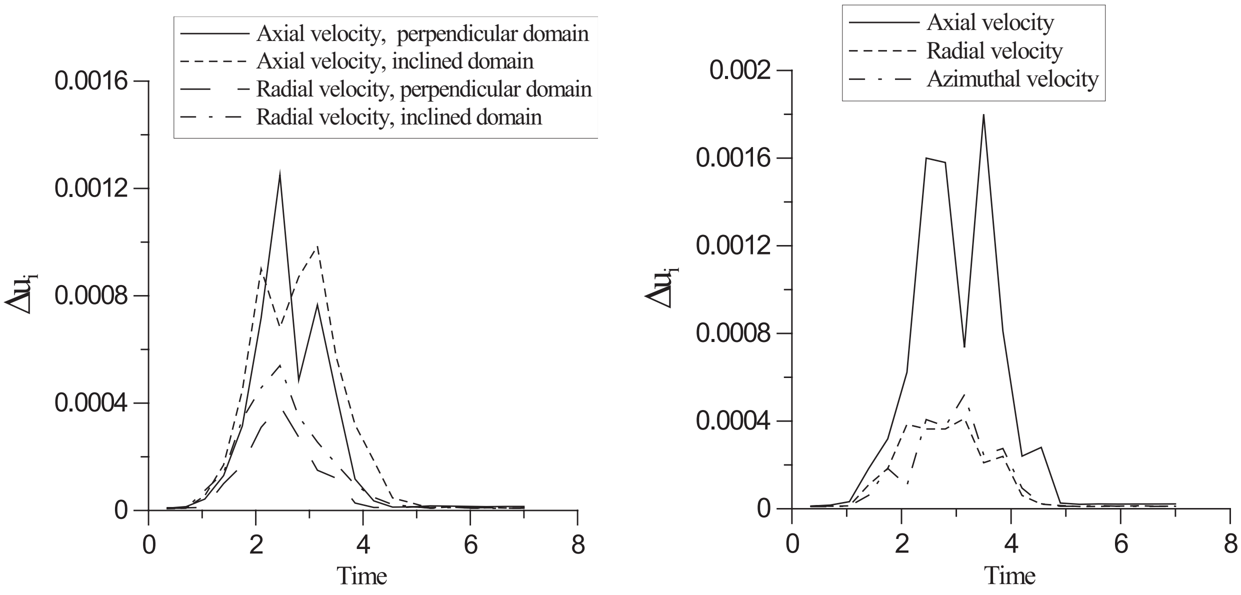

(a) Rectangular low Mach number code domain.

(b) Cylindrical low Mach number code domain.

Figure 6. Maximum discrepancy between velocity components for convecting Taylor vortex.

It can be noticed that for the cylindrical domain the maximum difference does not exceed 0.2% and for the rectangular domain it is even less. Maximum error of 0.002 is comparable to the value of $M_\infty^2 = 0.0025$.

Error of the order of M_∞^2 is an inherent error due to the difference between the solution of low Mach number equations and the solution of compressible equations with small but finite M_∞.

Test cases described above show that:

1. Compressible code and low Mach number code give very close numerical solutions when the Mach number of the physical problem is small.
2. Method of supplying boundary conditions from compressible to low Mach number code shows good performance.

B. Implementation of the coupling procedure

The implementation of the coupling procedure was tested using the problem of the convecting Taylor vortex was again considered. Computational domain for this test case is shown at Figure 7. All distances are non-dimensionalized by the initial radius of Taylor vortex R_T.

Low Mach number code domain is located at the left of the compressible code domain with the region of overlap between $x = 0$ and $x = 7.7$. A uniform free-stream with velocity parallel to x-axis $\vec{v}_\infty = (U_\infty, 0, 0)$ is taken as the undisturbed flow. This uniform flow is specified at the bottom and top boundaries of both domains. Reynolds number is $U_\infty R_T/\nu = 330$. Mach number $M_\infty = 0.15$ is used in the compressible code.

Disturbances in the form of a circular Taylor vortex (Eq. 1) are superimposed on the uniform flow. Initial coordinates of the center of a vortex are $(-13.55, 7.58)$, i.e. to the left from the inflow boundary of the low Mach number code domain ($x = -9$). Therefore, Taylor vortex is supplied through the inflow boundary of the low Mach number code domain and is convected with the uniform main stream. The moment when the vortex is completely inside the overlap region is shown in Fig. 7. Outflow boundary of the low Mach number code domain ($x = 7.7$) gets information from compressible code according to the method described in subsection II C 2. Inflow boundary for the compressible code ($x = 0$) obtains variables from low Mach number code as described in subsection II C 1.

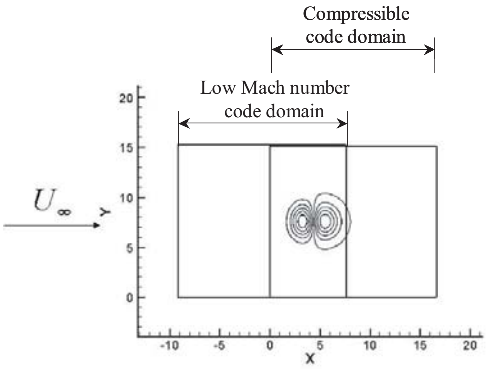

Figure 7. Computational domain for testing the coupling procedure. Vertical velocity contours are shown.

Good performance of boundary conditions supplied from compressible to low Mach number code was revealed in section A, where the low Mach number code domain was fully surrounded by the compressible code domain. The present setup, however, allows the performance of boundary conditions supplied from low Mach number to compressible code to be tested.

The quality of numerical solution of the compressible code can be judged by looking at the levels of the dilatation. From Eq. 1 we can find the dilatation of the Taylor vortex as

$$\texttt{div}\vec{v}' = \frac{1}{r}\frac{\partial}{\partial r}(r v'_r) + \frac{1}{r}\frac{\partial v'_\phi}{\partial \phi} + \frac{\partial v'_z}{\partial z} = 0, \tag{5}$$

since $v'_r = v'_z = 0$ and $\frac{\partial v'_\phi}{\partial \phi} = 0$.

In the inviscid formulation, Taylor vortex simply convects with the main flow. Viscous effects actually generates weak dilatation.[24] However, for the present disturbance level of 1% we can consider the linearized problem and write the solution as $\vec{v} = \vec{v}_\infty + \vec{v}'$ using the principle of superposition. The dilatation of the superposed (linearized) solution should also therefore be zero. Another idealization comes from the fact that Taylor vortex is the solution of the incompressible equations, but a finite Mach number $M_\infty = 0.15$ is used in the compressible code. However, this Mach number is still small enough and we can expect the analytical values for the dilatation to be non-significant.

Therefore, we can judge the accuracy of the boundary conditions by looking at the dilatation levels of the numerical solution of compressible code as the vortex is entering the computational domain.

First, the solution of the uncoupled problem was obtained as a reference case. Low Mach number code was not running. Disturbances (u', v') at the inflow boundary of the compressible code were calculated from the Eq. 1, where

$$t = t_0 + t', r = \sqrt{(x - x_0 + u_\infty t')^2 + (y - y_0)^2}. \tag{6}$$

t_0 is initial time specified in the beginning of the calculations to set initial radius of the vortex R_T; t' is time passed from the beginning of the calculations; (x_0, y_0) are coordinates of the initial position of the vortex center; $u_\infty t'$ is the distance which vortex traveled due to the convection.

Three possibilities for the inflow boundary conditions were considered, which are summarized in Table 1:

A Velocity components are set according to $\vec{v} = \vec{v}_\infty + \vec{v'}$. Temperature is set to T_∞, density is calculated from the continuity equation.

B Velocity components and temperature are the same as in method A, but density is strictly set to ρ_∞ instead of being calculated from the continuity equation.

C Boundary conditions based on locally one-dimensional Riemann invariants formed from $\vec{v}_\infty + \vec{v'}, T_\infty, \rho_\infty$ and variables interpolated from the interior of the domain are considered.[16]

Maximum dilatation in the compressible domain is plotted versus x-coordinate through the center of the vortex in Figure 8(a) for all three methods. When the center of the vortex is far to the left from the compressible domain, dilatation levels are practically zero, corresponding to the uniform flow. Dilatation reaches its maximum when the vortex center crosses the inflow boundary $x = 0$ for the methods B and C. This is due to the noise coming from the inflow boundary conditions. When disturbances are convected downstream further from the inflow boundary, dilatation levels come back to negligible value, which shows that numerical scheme holds the analytical value of almost zero dilatation pretty well. Method A (with density calculated from the continuity equation) performs the best when disturbances are crossing the inflow boundary. However, after disturbances have gone through and the inflow approaches the uniform state, the method becomes unstable. Boundary conditions based on Riemann invariants show the largest dilatation levels when disturbances are entering the domain. Method B, when all variables are strictly enforced, seems to give the best results for this test case. Note, however, that strictly speaking method B is overposed for uncoupled compressible flow. However, in the application of interest the low Mach number and the compressible domains are fully coupled. The "interface" is an interior region and full transfer of all variables is physically justified. Therefore, method B was used for supplying boundary conditions from low Mach number to compressible code in the coupled formulation.

Two variations of method B are possible when $\{\rho, u, v, w, T\}$ are supplied from low Mach number to compressible code (see Table 1). They reflect two different ways of specifying the density.

B1 Density for compressible code is interpolated from the density of low Mach number code $\rho^{compr} = \rho^{lowMach}$.

B2 Density for compressible code is calculated through the equation of state from the pressure, which is interpolated from the low Mach number code: $\rho^{compr} = P^{lowMach}/RT^{compr}$, where R is the gas constant.

Both of these methods were investigated, and dilatation levels obtained for the coupled problem are plotted in the Figure 8(b) together with the method B of uncoupled problem.

Uncoupled problem		*Coupled problem*	
A	$\vec{v}, T_\infty$ specified, ρ – from continuity	B1	$\rho^{compr} = \rho^{lowMach}$
B	$\rho, \vec{v}, T_\infty$ specified	B2	$\rho^{compr} = P^{lowMach}/RT^{compr}$
C	Riemann invariants		

Table 1. Methods for specifying inflow boundary conditions

First, one can notice that maximum dilatation is reduced for the coupled problem compared to the uncoupled problem. This is probably due to the fact that inflow disturbances calculated from Eq. 1 using

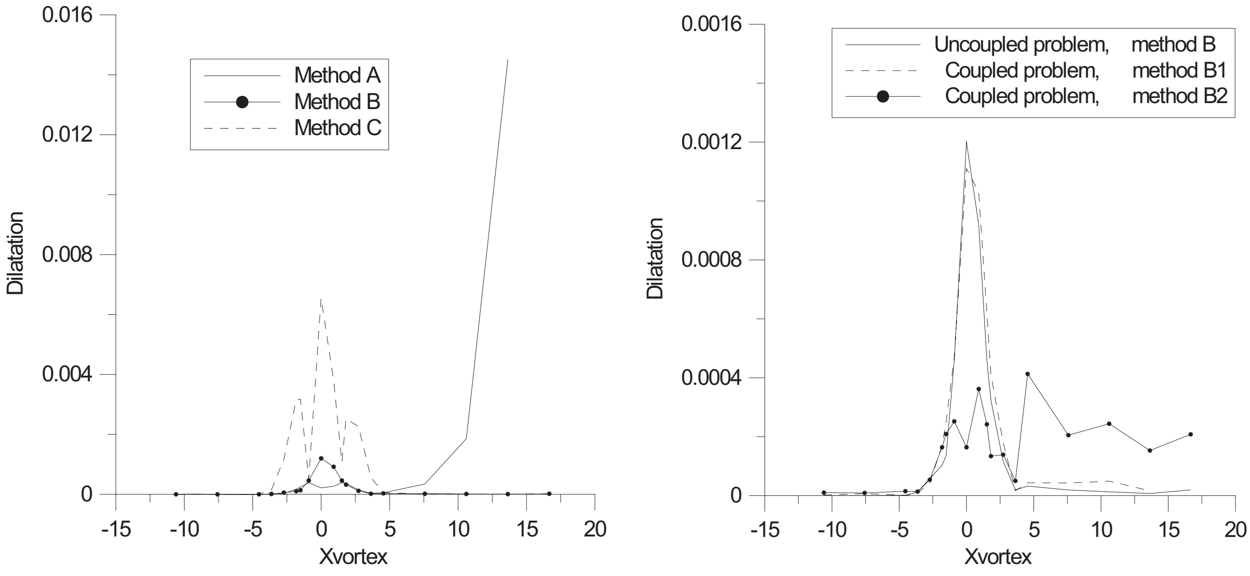

(a) Uncoupled problem.

(b) Coupled problem.

Figure 8. Dilatation levels in the compressible code versus x-coordinate of the vortex center.

Eq. 6 are worse approximation than disturbances calculated numerically by low Mach number code. When we compare the two variants of the method B for the coupled problem, we note that variant B2 (with density calculated from the pressure through the equation of state) performs better than the variant B1 when disturbances are crossing the domain, but fails to come back to zero-dilatation level when disturbances are convected away. Therefore, variant B1 of method B, which is a simple interpolation of all five variables $\{\rho, u, v, w, T\}$ from low Mach number to compressible code gives the best overall performance. It was chosen as the basic method for supplying boundary conditions to the compressible code.

Maximum discrepancy between the components of velocity obtained by two codes for the coupled problem calculated with Eq. 2 is shown in Fig. 9. The difference in pressure calculated with Eq. 3 is again about two orders of magnitude smaller than difference in velocity and not plotted here.

The difference between solutions for the fully coupled problem is even smaller than the difference for one-way coupled problem (see subsection III A 2), which is probably due to the fact that two-way coupling enables simultaneous adjustment of solutions of two codes to each other through a feedback mechanism. It is worth noting that maximum discrepancy does not show a distinct peak as dilatation levels do, but stays at about the same level over the whole period when vortex is inside the computational domain. This is because the maximum discrepancy is caused by the difference of equations being solved, and not by the performance of the boundary conditions. Therefore, maximum discrepancy does not depend on the relative position between the vortex and the boundaries and is about the same for the whole period of vortex passing.

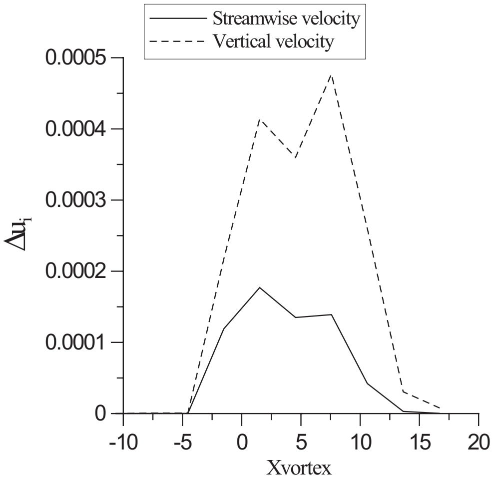

Figure 9. Maximum discrepancy for the coupled problem.

Vertical velocity along the horizontal line passing through the center of the vortex is plotted at Fig. 10 for the coupled calculation as well as for single calculations performed with low Mach number and compressible code, respectively. Plots for three relative positions of the vortex are shown: when it crosses the compressible code domain ($x_{vortex} = -1.5$, Fig. 10(a)), when it is in the center of the overlap region ($x_{vortex} = 4.55$, Fig. 10(b))and when it exits the low Mach number code domain ($x_{vortex} = 10.6$, Fig. 10(c)).

When the vortex is far to the left from the outflow boundary of the low Mach number code domain, the difference between all four solutions is very small (Figs. 10(a) and 10(b)). However, difference between the single compressible solution and the two coupled solutions is larger than the difference among the coupled solutions. It is consistent with our earlier observation that solutions are closer when the codes are allowed to communicate through the feedback mechanism and that inflow boundary conditions for the compressible code perform better in the coupled case.

However, if we look at the profiles when the vortex is leaving the low Mach number code domain, we see some oscillations in the coupled solution calculated with the low Mach number code. These oscillations are due to the influence of the outflow boundary conditions in the low Mach number code on the solution. It is interesting to note, that performance of a single low Mach number code with convective outflow boundary conditions for the vortex leaving the domain[18] is even worse. Not only oscillations do not reduce in this case, but also the mean value of the vertical velocity is significantly altered. This shows that the present coupling procedure provides a good alternative to specifying approximate outflow boundary conditions for the case of outgoing disturbances. To assess the influence of grid size on the performance of outflow boundary conditions, another calculation of both coupled and single problems was performed. The number of grid points in the low Mach number code domain was increased from 128x128 to 256x256 with all other parameters of the calculation left the same. Vertical velocity profiles for the vortex exiting the low Mach number code domain are plotted in Fig. 10(d). It can be seen that the magnitude of oscillations is reduced from 10^{-3} to 10^{-6} for the coupled problem, showing the vast improvement of the performance of outflow boundary conditions with the grid size. In the single code calculation, oscillations are also significantly reduced with grid refinement, but velocity profile deviates even further from the correct one, showing the fundamental drawback of the convective outflow boundary conditions in the low Mach number code for the outgoing disturbances.

The reason we did not see any significant oscillations when the vortex was exiting the low Mach number code domain in subsection III A 2 is that the same number of grid points 128×128 was used for much smaller low Mach number code domain (1.5×4.5 in units of R_T as opposed to 16.67×15.15 in the present case). However, when the grid size was reduced from 128×128 to 32×128 in the calculations of subsection III A 2, some oscillations became noticeable, especially for the cases of inclined and cylindrical domain. These observations suggest that the minimum grid size requirement exists

$$\Delta x / L_d < 0.05 \tag{7}$$

(where L_d is the disturbance scale) in order for the oscillations in the low Mach number code due to the outflow boundary conditions to be less than 0.1% of the mean value within the present coupling procedure .

IV. Calculations of jet in a crossflow

A. Literature review

Jet in a crossflow (JCF) can be considered as a technically relevant test problem before studying real film-cooling flows. The only difference between JCF and film-cooling flows, besides geometry, is that the temperature and the density of a jet and a crossflow are taken to be the same, while in film-cooling flows they are different. Though the difference in temperature and density definitely leads to the quantitative differences between two types of flows, many fundamental features of these flows are similar since they are caused by misalignment of momentum, rather than by mismatch in temperature and density.

Jets in crossflow are thoroughly investigated and well documented over past years, providing reliable information for comparison with numerical results. This makes this problem suitable for testing the present computational method. There are three non-dimensional parameters pertinent to the JCF problem: jet Reynolds number $U_{jet} d/\nu$, crossflow Reynolds number $U_\infty \delta/\nu$ and blowing ratio defined as $R = U_{jet}/U_\infty$ when $\rho_{jet} = \rho_\infty$ (here d is the jet diameter and δ is the crossflow boundary layer thickness). Many researchers have investigated cases of high blowing ratio greater than two.[25,26,27,28] However, high blowing ratio is representative of a different application of jets in crossflow, namely, dilution holes of gas-turbine combustors. Blowing ratio less than two are used in film cooling applications to keep the injected cold gas close to the surface. Among experimental investigations of jets in crossflow with small blowing ratio there are experiments of Gopalan et al.,[29] Peterson et al.[30,31] and Gamussi et al.[32] Gopalan et al. considered turbulent jets with flow Reynolds number $U_\infty d/\nu = 19000$, Peterson et al. were also looking at turbulent jets but emanating

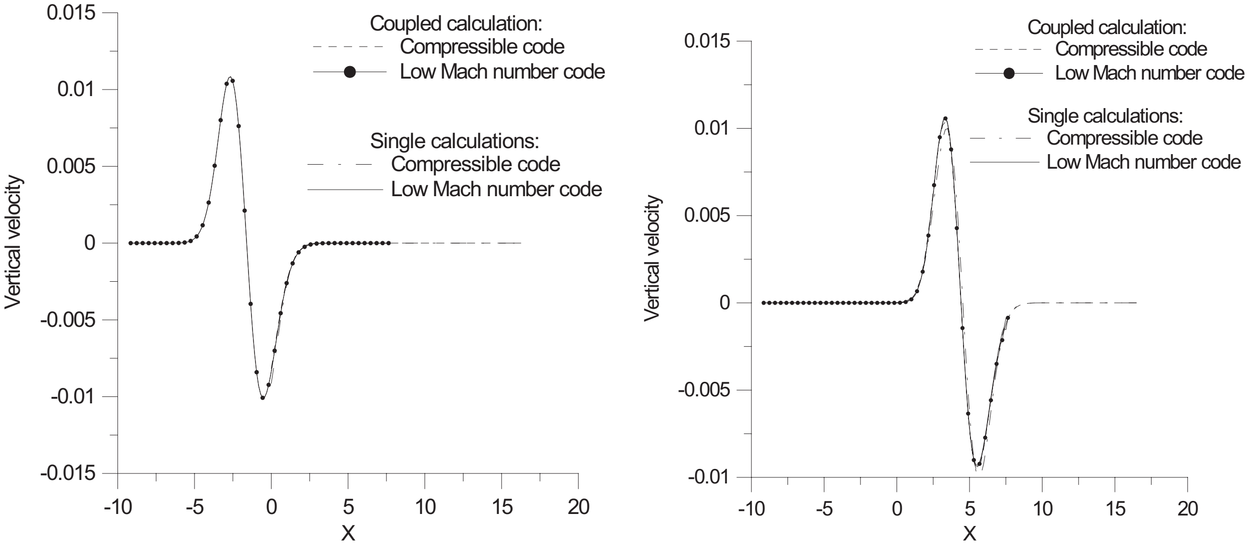

(a) Vortex crosses compressible domain, $x_{vortex} = -1.5$.

(b) Vortex in the middle of overlap, $x_{vortex} = 4.55$.

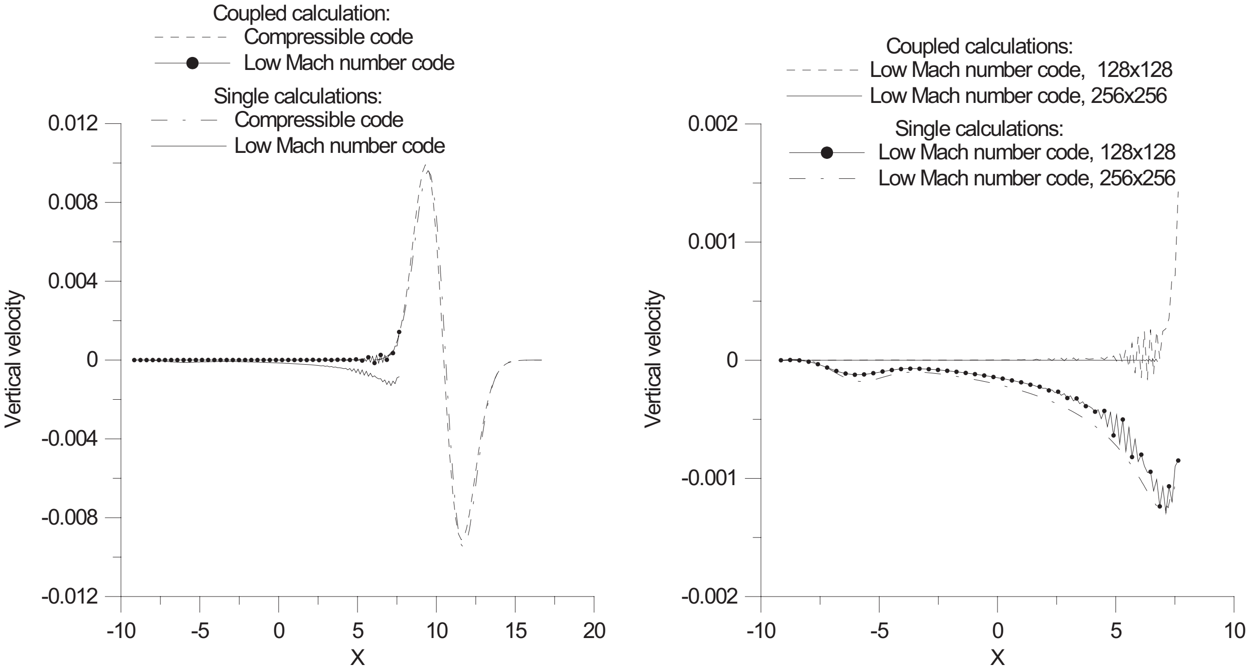

(c) Vortex exits low Mach number domain, $x_{vortex} = 10.6$.

(d) Vortex exits low Mach number domain, grid size variation.

Figure 10. Vertical velocity along the horizontal line through the center of the vortex.

from the very short delivery tubes where the plenum configuration was a significant parameter. Gamussi et al. were looking at laminar jets with very low Reynolds number $U_\infty d/\nu = 100$.

There also exists many numerical investigations of JCF problem. Among them is Direct Numerical Simulations of Muppidi et al.[33] who looked at the influence of the jet velocity profile and the crossflow boundary layer thickness on the jet trajectory at two different velocity ratios. One of their velocity ratios is 1.52, which is characteristics of film-cooling applications. The case I of Muppidi et al. (see Table I of Ref. 33) was chosen for comparison with the results of the present computational method.

B. Geometry and boundary conditions

Schematical configuration of the JCF problem is shown at the Fig. 11. Jet with diameter d issues perpendicular to the crossflow. Jet Reynolds number $Re_j = U_j d/\nu = 1500$, where U_j is the jet bulk velocity; blowing ratio $U_j/U_\infty = 1.52$. Characteristics of the crossflow are as follows: 80% boundary layer thickness at the inflow $\delta_{80\%} = 1.32d$, which gives crossflow Reynolds number $U_\infty \delta_{80\%}/\nu = 1300$. Mach number $M_\infty = 0.15$ is used for the crossflow in the present simulation, which is different from $M_\infty = 0$ in incompressible calculations of Muppidi et al.[33] According to the non-dimensional parameters, both jet and crossflow are in laminar regime.

Projection of the full computational domain onto $x-y$ plane is shown in the Fig. 12. It consists of the low Mach number code domain and the compressible code domain.

1. The low Mach number code domain

Cylindrical domain with diameter d and height $2.2\,d$ is used for the calculation of the jet by the low Mach number code. The domain extends $2\,d$ below the crossflow surface, and $0.2\,d$ above, so that cylindrical region of overlap with compressible code domain exists with diameter d and height $0.2\,d$ (see the enlarged view of the region of overlap in the Fig. 12(b).) Grid of $94 \times 64 \times 64$ points with uniform distribution in streamwise, radial and circumferential directions, respectively, is used. This gives maximum cell size of $0.02\,d \times 0.008\,d \times 0.05\,d$, which satisfies the resolution requirement given by Eq. 7. Jet parabolic profile is specified at the inflow of the domain $2\,d$ below the crosfflow surface. No-slip boundary conditions are used at the pipe walls, which extend from the jet inflow to the crossflow surface. Boundary conditions described in subsection II C 2 are specified at the "free" boundaries, corresponding to the boundaries of the overlap region.

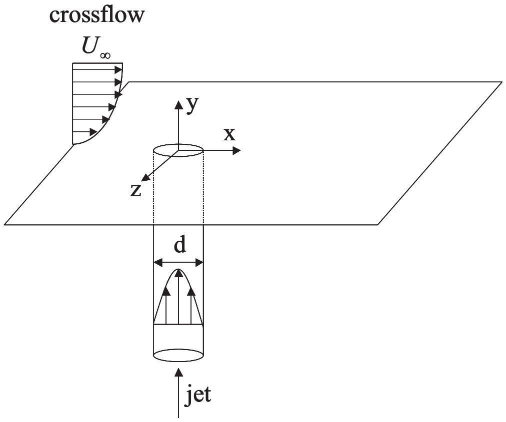

Figure 11. Schematics of the jet in crossflow problem.

2. The compressible code domain

Cartesian domain with dimensions $30\,d \times 10\,d \times 3\,d$ is used for the calculation of the crossflow by the compressible code. Computational grid with $204 \times 144 \times 51$ grid points is used. Grid is clustered at the region of jet injection as well as at the crossflow boundary layer. Clustering is designed so that the fine grid approximately follows the jet trajectory before it is turned by the crossflow. Every 4^{th} point in streamwise direction and every 10^{th} point in vertical direction is shown in the Fig. 12(a), every point is shown at the enlarged view of Fig. 12(b). Grid is uniform in spanwise direction. Boundary layer profile is specified at the inflow located about $10\,d$ upstream of the jet. No-slip and isothermal boundary conditions are used at the bottom wall with density obtained from the continuity equation. Wall temperature is set equal to $T_{0\infty} = (1 + \frac{(\gamma-1)}{2} M^2)\, T_\infty$. Values interpolated from the low Mach number code according to the method described in subsection II C 1 are specified at the place of jet injection. Parameters calculated at the edge of the boundary layer are set at the top of the computational domain. At the outflow, located $20\,d$ downstream of the jet injection, parabolized Navier-Stokes equations are solved. In the spanwise direction, periodic boundary conditions are applied. Since spanwise length of the domain is $3\,d$, the present configuration corresponds to the periodic array of film-cooling holes with the pitch of $3\,d$. This configuration is different from the case of a free jet calculated by Muppidi et al.[33]

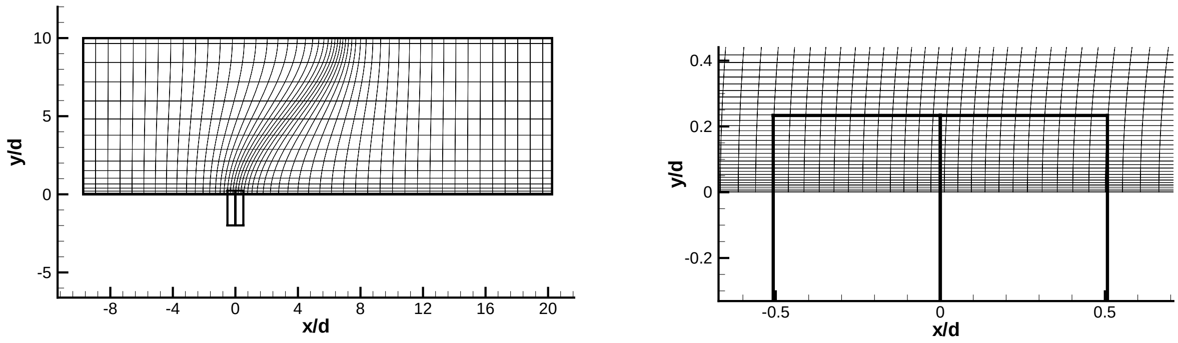

(a) The whole domain.

(b) Enlarged view of the overlap region.

Figure 12. Projection of the computational domain onto $x - y$ plane.

Calculations are initialized as follows. First, the steady solution for the crossflow boundary layer in absence of the jet is obtained. This solution is interpolated into the low Mach number code domain, so that the region of overlap in the low Mach number code also gets initial conditions corresponding to the crossflow boundary layer. Then jet is slowly turned on, so that the jet bulk velocity changes in time corresponding to the formula

$$U_j = \left\{ \begin{array}{ll} U_j^{max}\, t/t_{lag} & \text{if } t < t_{lag} \\ U_j^{max} & \text{otherwise} \end{array} \right. .$$

Here t is the computational time, t_{lag} is the time lag equal to $2\,d/U_\infty$ and U_j^{max} is the final bulk velocity. Without the slow injection, disturbances suddenly supplied to the compressible code would be too large leading to numerical instability. Solutions are advanced in time with the computational time step $0.01\,d/U_\infty$.

C. Simulation results

1. Vortex systems of jet in a crossflow

Basic coherent structures or vortex systems of JCF are described by many authors.[27, 25, 32, 26] The primary feature of jets in crossflow is counter-rotating vortex pair (CRVP). CRVP is created in the near field and occupies the entire cross-section of the jet, giving it the "kidney" shape. It carries streamwise-oriented vorticity. The length scale of CRVP is significantly greater than that of the turbulence, so CRVP is more a feature of the mean flow than the turbulence.[30] CRVP signature is observed far downstream from the jet injection, where the other vortex systems are diffused. Among other coherent structures is the horseshoe vortex system (HSV), which occurs upstream of the jet and close to the wall and is formed due to the blockage of the crossflow by the jet. Ring-like vortices (RLV), or shear-layer vortices with transverse vorticity are formed on the lateral edges of the jet. Ring-like vortices are unsteady structures, contrary to CRVP and HSV.

Many researchers who conducted experiments on jets in crossflow varying the blowing ratio noticed that the evolution of vortical structures is qualitatively different for different blowing ratios.[32, 26, 25, 27, 29] Some of the authors observed the existence of two kinds of regimes: low-R and high-R regime, where R is the blowing ratio.[32, 26, 29] $R \sim 2 \div 3$ was found as a dividing line between two regimes, most likely depending on the other non-dimensional parameters describing the flow. One of the significant differences between two regimes is the structure of the wake region of the jet right above the wall. For small blowing ratio, the large zone of reverse flow occurs to the right of the jet injection. It is called the "dead zone" by Gopalan et al.[29] and DSSN vortices (downstream spiral separation node) by Peterson et al.[30] DSSN vortices are steady and spatially stationary. For high blowing ratio, the formation of the "dead zone" is not observed, but instead the unsteady vortices of alternating sign are formed by the roll-up of wall boundary layer fluid. These "wake" or "upright" vortices are described in details by Fric and Roshko[27] and Kelso et al.[25] These structures are generally not noticed for blowing ratios below two.

Another reported common feature of jets in crossflow at small velocity ratios is the existence of three-dimensional "hairpin" vortical structures.[13, 26, 32, 29] It is believed that other vortical systems observed in low-R jets (CRVP, RLV and wall-normal vortices) constitute the base, the top part and the legs of the "hairpin" structures, respectively. Blanchard et al.[26] attributes formation of the "hairpin" structures to the elliptical instability of CRVP. Gamussi et al.[32] proposes the mechanism of pairing of two counter-rotating longitudinal vortex tubes to form a single three-dimensional structure. Gopalan et al.[29] hypothesizes that stretching of the jet vortex ring in vertical direction is a formation mechanism for the "hairpin" structures, which he calls "semi-cylindrical vortical layer" in his paper. No "hairpin"-type structures were reported in high-R experiments. The reason for the substantial difference in jet vortical structures at small and high blowing ratios is still the subject of ongoing research.

2. Vorticity dynamics of the present calculations

In this section we try to identify vortical structures described above in the present calculations. Although the current calculations use spanwise periodic boundary conditions and strict comparison with previous work on isolated JCF is not possible, it is still useful to make qualitative comparison.

To look at vorticity dynamics of the present calculations, we plot vorticity and streamlines at different cross-sections. Instantaneous and time-averaged normalized transverse vorticity $\omega_z\, d/U_\infty$ in $x-y$ plane taken through the center of the jet $z/d = 0$ is plotted in Figure 13(a) and Figure 13(b). We call this plane a center-plane in the present discussion. Only compressible code domain is shown for the sake of clarity. In the time-averaged field, only two shear layers at the lateral edges of the jet are visible, and no vortices are present. This confirms the fact that transverse vortices are non-stationary and unsteady structures. Instantaneous transverse vorticity field is much more complex, showing at least three rows of transverse vortices. Instantaneous and time-averaged in-plane velocity $\sqrt{u^2+v^2}$ and streamlines are plotted in Figure 14(a) and Figure 14(b). Both compressible and low Mach number code domains are shown. Looking at both instantaneous and time-averaged streamlines one can notice the node point. It looks like streamlines are originating from this point and diverging in all directions. The similar node point is shown in Figure 16 of Kelso et al.[25] for R=2.2 and in Figure 5(a) of Muppidi et al.[33] for the same flow regime as present calculations. The location of the node is $(x/d \sim 0.83, y/d \sim 0.27)$, which is close to $(x/d \sim 1.05, y/d \sim 0.3)$ cited by Muppidi et al.[33] It is interesting to note that the windward and leeward sides of the jet eventually collapse in the vertical center-plane. Instantaneous streamlines show the oscillations of the jet trajectory as well as formation of unsteady transverse vortices. The enlarged view of time-averaged steamlines is shown in Figure 15(a). The horseshoe vortex is seen upstream of the jet with clockwise rotation. It is located at $(x/d = -0.82, y/d = 0.11)$ which is a little bit closer to the jet than $x/d = -1.4$ found by Muppidi et al. Hovering vortex is also observed just above the jet exit near the leading edge, consistent with observations of Muppidi et al.[33] and Kelso et al.[25] Hovering vortex is only resolved in the low Mach number code domain, since the size of the grid Δx in the compressible code domain is about five times larger than in the low Mach number code domain in the region of jet injection. This is because the length of the compressible code domain is $30\,d$, thirty times larger than that of the low Mach number code domain. Time-averaged steamlines in compressible code domain are shown in Figure 15(b) with no hovering vortex. This explains the fact that hovering vortex in our coupled simulations extends vertically only up to to $y/d \sim 0.2$, where the low Mach number code domain ends. It persists up to $y/d \sim 0.75$ in calculations of Muppidi et al.[33] One can notice the intersection of streamlines just above the hovering vortex in Fig. 15(a) since streamlines are calculated from two different flowfields – one with the hovering vortex, and the other - without it. Muppidi et al. used incompressible code similar to the present low Mach number code everywhere. Incompressible code is computationally much less expensive than the fully compressible one, which allowed Muppidi et al. to keep the resolution higher than in the present calculations. This observation suggests that the resolution of the compressible code in the region of the jet injection must be increased in order to capture the near-wall structures.

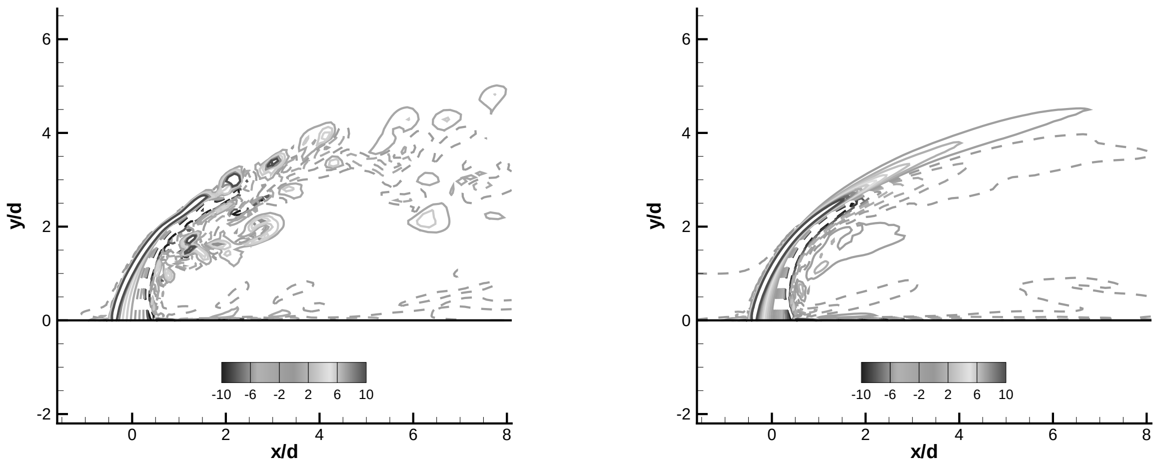

(a) Instantaneous vorticity.

(b) Time-averaged vorticity.

Figure 13. Transverse vorticity, $\omega_z\, d/U_\infty$. $x - y$ plane, $z/d = 0$. Solid lines – positive vorticity, dashed lines – negative vorticity.

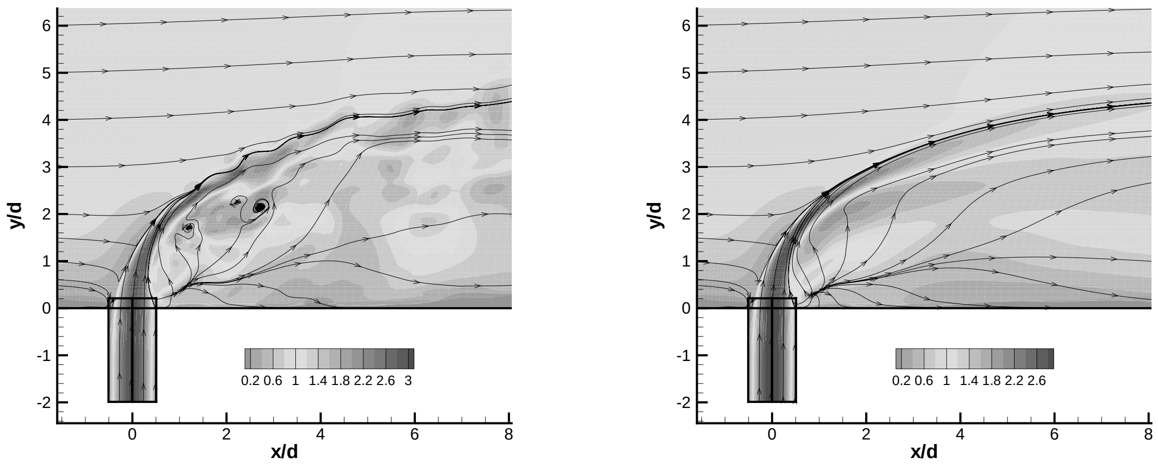

(a) Instantaneous flow-field.

(b) Time-averaged flow-field.

Figure 14. In-plane velocity, $\sqrt{u^2 + v^2}$, and streamlines. $x - y$ plane, $z/d = 0$.

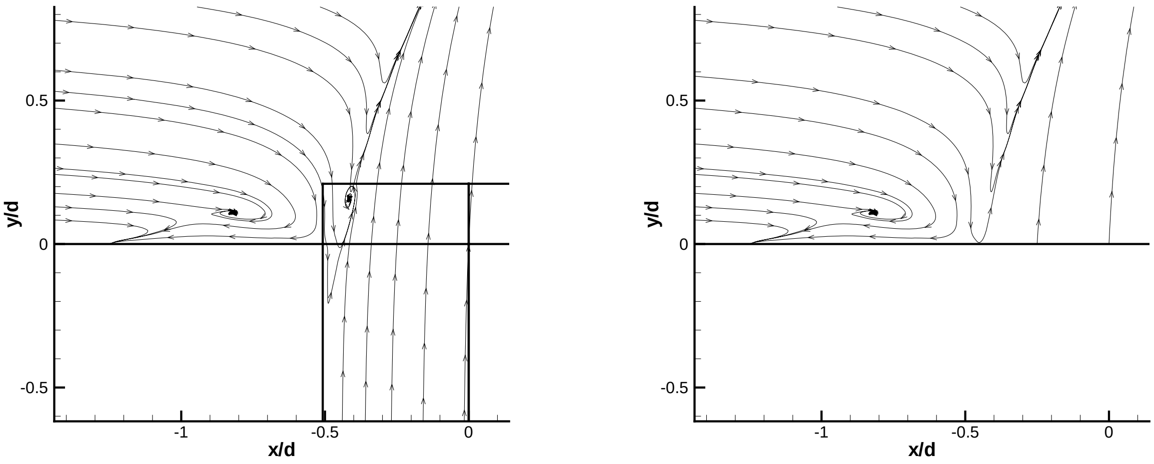

(a) Compressible and low Mach number code domains.

(b) Only compressible code domain.

Figure 15. Time averaged streamlines. $x - y$ plane, $z/d = 0$. Enlarged view.

In order to determine the path of the jet fluid, we plot three-dimensional time-averaged streamlines originating from the various parts of the jet in Figure 16(a). Five streamlines originating at the the center-plane (–0.1,0,0), (0,0,0), (0.1,0,0), (0.2,0,0) and (0.3,0,0) follow the jet trajectory, which is defined as the streamline originating from the center of the jet exit by Muppidi et al. However, four streamlines originating off the center-plane (0,0,–0.5), (0,0,–0.1), (0,0,0.1) and (0,0,0.5) follow much lower trajectory and occupy the region which might be called the wake of the jet. The off-center-plane jet fluid follows lower trajectory since it faces stronger cross-flow, which experiences less blockage by the jet. Two streamlines which are coming from the leading edge of the jet (–0.45,0,–0.005) and (–0.45,0,0.005) bend around the jet together with the crossflow, since they don't have enough momentum to resist the crossflow and follow the jet trajectory. If we look at the $x - z$ projection of the three-dimensional streamlines in Fig. 16(b), we see that the center-plane jet fluid following the jet trajectory stays in the center-plane. The off-center-plane fluid is gathered at about $z/d \sim \pm 1$, which are the lateral boundaries of the jet wake. Fluid coming from the leading edge of the jet is lifted with the crossflow. It almost reaches the center-plane at $x/d \sim 1.5$, but later merges with the lateral boundaries of the wake. The $y - z$ projection of the trajectories (Fig. 16(c)) shows that all the jet fluid not coming from the immediate vicinity of the jet centerline is gathered into the CRVP, whose vertical and spanwise extent coincides with the extent of the jet wake.

In order to extract three-dimensional coherent structures, the isosurface of the Laplacian of pressure $P_{k,k}$ corresponding to a positive value of 5 is plotted in Figure 17 together with three-dimensional streamlines. Since the vortex cores are associated with strong vorticity and local pressure minima, it can be shown that positive isosurfaces of $P_{k,k}$ can be used to identify coherent structures.[13] Coherent structures similar to the hairpin vortices observed by other authors are visible. It appears that two layers of hairpin vortices are present – above the wake region and in the wake region. The structures above the wake region have their top parts linked to the jet trajectory. The lower structures are located just below the upper structures with their legs penetrating the wake region. Streamwise-oriented vortex tubes are scattered in the region of the wake corresponding to the streamwise vorticity carried by CRVP. $x - z$ and $y - z$ projection of coherent structures are shown in Fig. 18(a) and Fig. 18(b), respectively.

To investigate the path of the cross-flow fluid, three-dimensional streamlines originating from the different parts of the crossflow are plotted in Figure 19(a). A streamline coming from the center of the jet is also shown to outline the jet trajectory. Several streamlines originating very close to the center-plane plane $(z/d\ \pm 0.01)$ at different distances from the wall are shown. Streamlines originating at $y/d = 2$ and higher in the crossflow merge with the jet. Streamlines coming from $y/d = 1.5$ go around the jet deflecting only slightly from the center-plane (see also $x - z$ view in Fig. 19(b)). Trajectories coming through $y/d = 1$ deflect

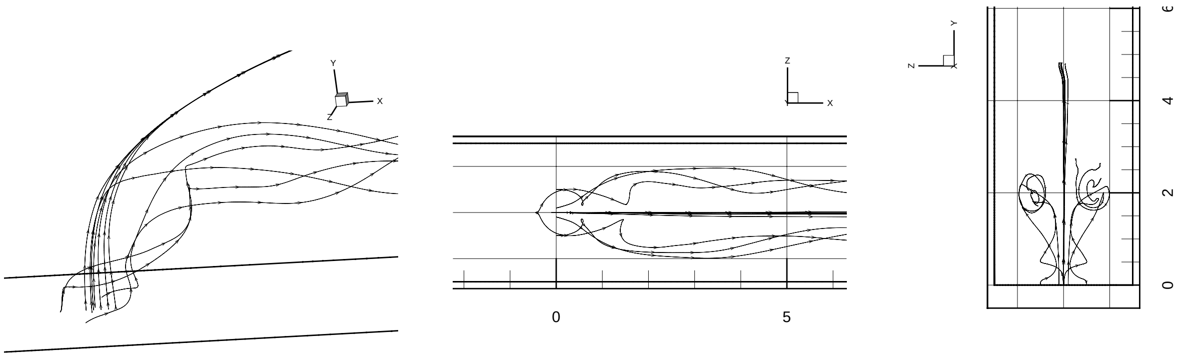

(a) Three-dimensional view.

(b) $x - z$ projection.

(c) $y - z$ projection.

Figure 16. Time-averaged three-dimensional streamlines originating from the jet.

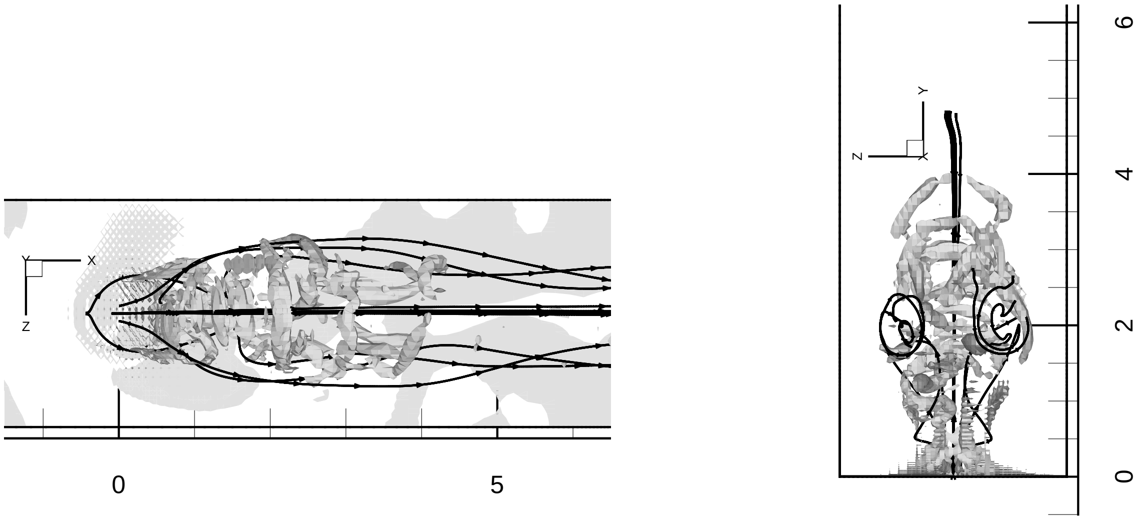

(a) $x - z$ projection.

(b) $y - z$ projection.

Figure 18. Isosurface of the Laplacian of pressure $P_{k,k} = 5$.

more and rise right behind the jet into the wake of the jet. Fluid originated from the crossflow boundary layer at $y/d = 0.5$ experiences reverse motion behind the jet and then uplift into the jet wake. This reverse motion behind the jet creates a node point observed in Fig. 14. Also, two streamlines caught up into the upstream horseshoe vortex are shown. They go wide around the jet and rejoin together at the center-plane at $x/d \sim 3.5$. Streamlines originating at $z/d > 0.1$ and $y/d < 2$ circle around the jet, then reverse back and rise into the wake of the jet, creating DSSN vortices noticed by Peterson et al.[30] These streamlines are not plotted here for the sake of picture clarity.

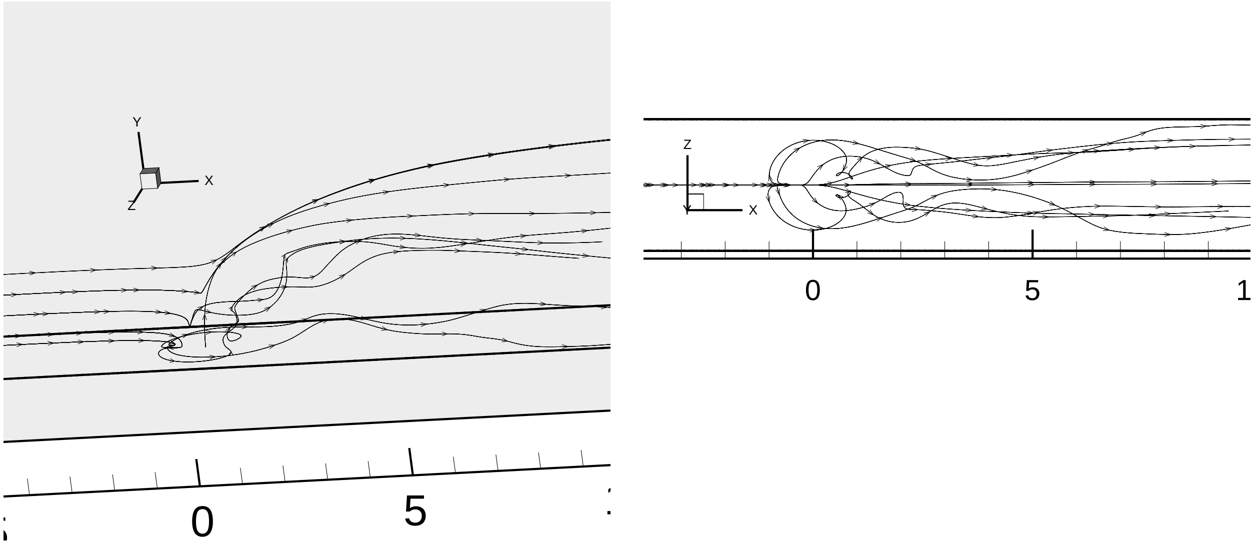

(a) Three-dimensional view.

(b) $x - z$ projection.

Figure 19. Time-avera **ıe crossflow.**

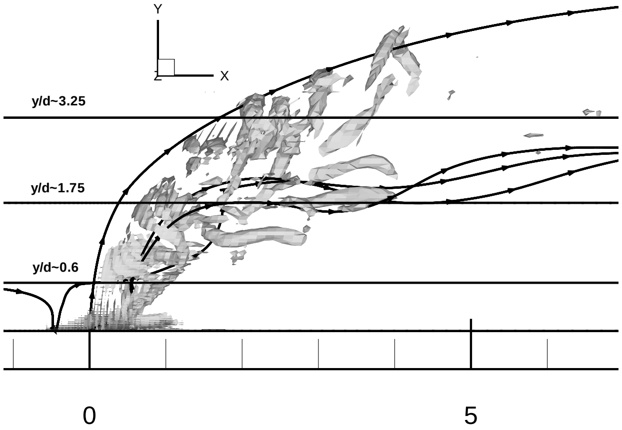

Figure 20. Horizontal cross-sections with respect to the coherent structures.

To complete the picture of JCF behavior, we look at instantaneous and time-averaged normalized vertical vorticity $\omega_y \, d/U_\infty$ as well as streamlines in the horizontal cross-sections. Location of used horizontal cross-sections with respect to coherent structures is shown in Fig. 20. Several streamlines originating from the center and the edges of the jet are also plotted to mark the wake region and the jet trajectory. DSSN vortices consisting of the crossflow recirculating behind the jet are revealed in Figure 21 in the horizontal plane $y/d \sim 0.6$. Notice that there is almost no difference between instantaneous (Fig. 21(a)) and time-averaged (Fig. 21(b)) vorticity, showing that DSSN vortices are spatially stationary and steady structures as was noted by Peterson et al.[30] Another node point as well as the recirculating flow is seen in the time-averaged streamline pattern (Fig. 21(c)). The horizontal plane coming through the wake of the jet $y/d \sim 1.75$ is shown in Figure 22. Instantaneous ω_y of only positive sign is found at $z/d \sim 1$ and only negative sign at $z/d \sim -1$ (Fig. 22(a)). This persistence in the vorticity sign is also reflected in the time-averaged vorticity pattern, where two distinct vorticity lobes of the same sign and approximately the same magnitude as instantaneous values are noticed (see Fig. 22(b)). The node point again exists in the streamline pattern (Fig. 22(c). The node point corresponds to the lift up of the crossflow fluid from below, which follows almost vertical path. Intersection of the vertical streamline with the horizontal plane appears as the point of origin for the in-plane streamline pattern. Therefore, existence of the node point in horizontal cross-section is an indication of the wake region, where fluid is being tackled from below. The horizontal plane passing through the legs of upper hairpin structures above the jet wake at $y/d \sim 3.25$ is shown in Fig. 23. Vorticity pattern is completely different here than in the wake region. Vortices of alternating sign are being shed on each side of the centerline $z/d = 0$, which is seen in Fig. 23(a) (contours of instantaneous vorticity). Averaged vorticity has mush smaller value than instantenous vorticity, showing that present vortical structures are of alternating sign and they mostly cancel each other during averaging (see Fig. 23(b)). Time-averaged streamline pattern does not

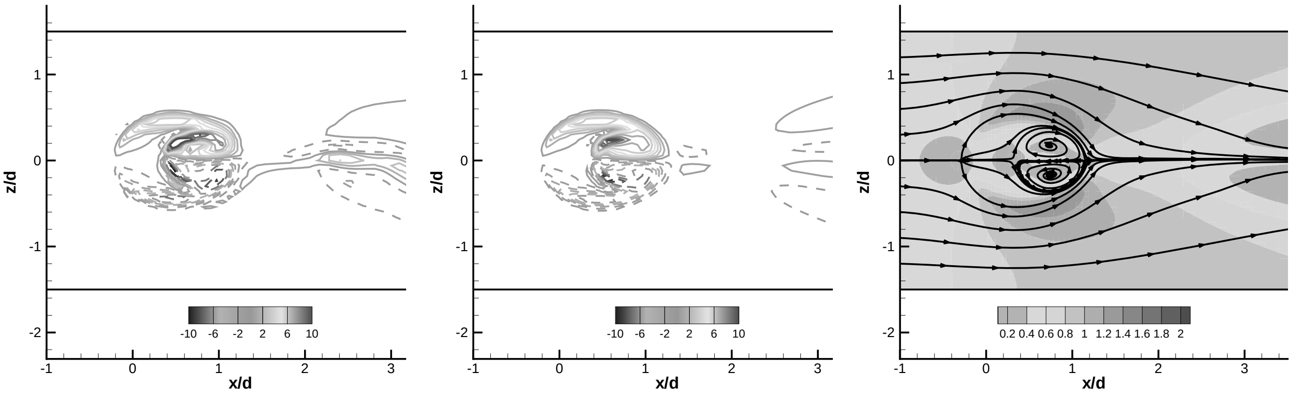

(a) Instantaneous vertical vorticity, $\omega_z\, d/U_\infty$.

(b) Time-averaged vertical vorticity, $\omega_z\, d/U_\infty$.

(c) Time-averaged in-plane velocity, $\sqrt{u^2 + w^2}$, and streamlines.

Figure 21. Horizontal cross-section, $y/d \sim 0.6$. Solid lines – positive vorticity, dashed lines – negative vorticity.

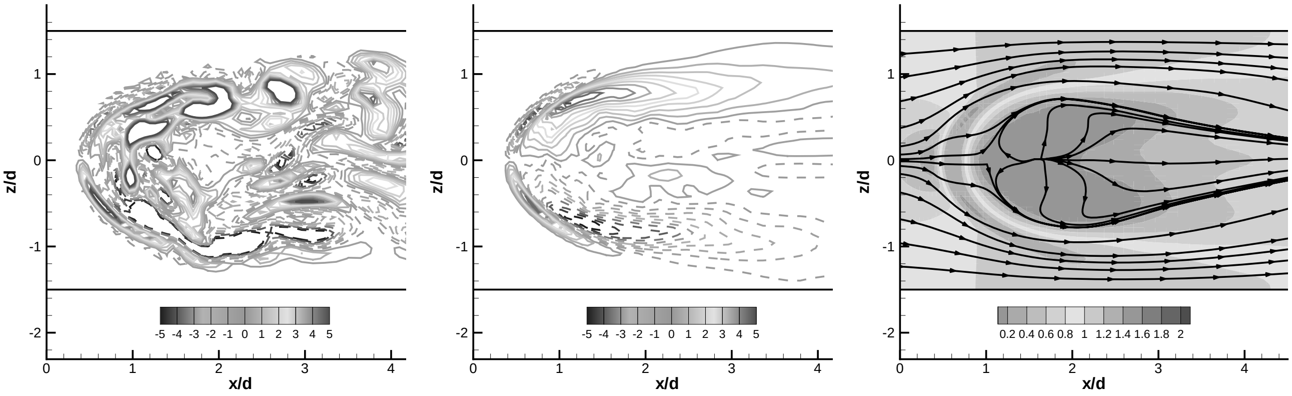

(a) Instantaneous vertical vorticity, $\omega_z\, d/U_\infty$.

(b) Time-averaged vertical vorticity, $\omega_z\, d/U_\infty$.

(c) Time-averaged in-plane velocity, $\sqrt{u^2 + w^2}$, and streamlines.

Figure 22. Horizontal cross-section, $y/d \sim 1.75$. Solid lines – positive vorticity, dashed lines – negative vorticity.

It is worth noting that coherent structures are only observed until $x/d \sim 5$, after which they suddenly disappear. The disappearance of coherent structures might be caused by the interactions among the jets which are separated by $3\,d$ in the spanwise direction in the present computations. To look at the spanwise

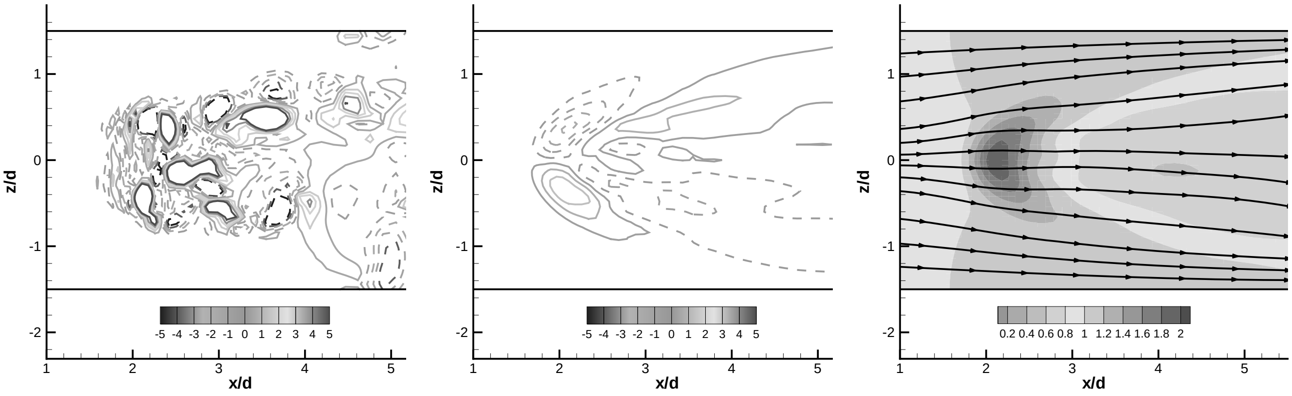

(a) Instantaneous vertical vorticity, $\omega_z\, d/U_\infty$.

(b) Time-averaged vertical vorticity, $\omega_z\, d/U_\infty$.

(c) Time-averaged in-plane velocity, $\sqrt{u^2+w^2}$, and streamlines.

Figure 23. Horizontal cross-section, $y/d \sim 3.25$. Solid lines – positive vorticity, dashed lines – negative vorticity.

development of the jet, temperature contours in the horizontal plane $y/d \sim 1.75$ are plotted in the Figure 24. Although temperature variations are reduced to minimum in the current computations, looking at temperature field is still a good way of flow visualization since temperature plays the role of a passive scalar introduced from a jet into crossflow. Oscillations of the lateral boundary of the jet wake are observable. The lateral boundary reaches the edge of the domain $z/d = 1.5$ at $x/d \sim 5$. Coherent structures characteristic of a single jet are destroyed after this point by the interactions with the neighboring jets.

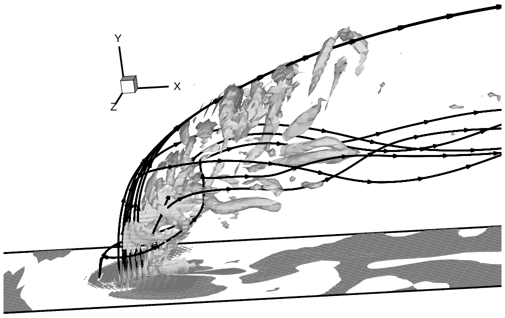

Figure 17. Isosurface of the Laplacian of pressure $P_{k,k} = 5$. Three-dimensional view.

3. Analysis of the vorticity dynamics

In this section we try to analyze the behavior of the vortical structures and their relations to each other. Jet fluid originating in the vicinity of the jet centerline follows the highest trajectory and stays in the center-plane. Two shear layers at the lateral edges of the jet are seen in the contours of instantaneous and time-averaged transverse vorticity (Fig. 13). When the jet trajectory starts oscillating, the vortices of alternating sign (with positive vorticity prevailing) are shed into the crossflow. These are the ring-like or shear-layer vortices observed by other researchers (they are also sometimes called upper and lower structures). These vortices follow the jet trajectory (a streamline originating from the center of the jet). They form the top parts of the upper hairpin structures. Plot of instantaneous vertical vorticity through the legs of upper hairpin structures shown in Fig. 23(a) reveals the alternating signs of the vertical vorticity in the legs. This is in agreement with the alternating sign of the transverse vorticity of the top parts, which confirms the fact that both these vortical tubes are parts of the same hairpin structure. Both transverse and vortical vortices of alternating sign as well as upper hairpin structures occur at $x/d \sim 2 \div 4$, which again proves their interdependence. Basic mechanism suggested in the literature for the development of hairpin structures during jet-crossflow interactions is the instability of CRVP.[26,32] It should be noted that the upper hairpin structures, linked to RLV and jet trajectory, can not be generated this way. First, the roll-up of streamwise vortical tubes into one coherent structure would suggest that the vorticity sign of two successive structures should be the same, and not alternating, as in the present case. Second, the upper hairpin structures occur much higher than the wake region, where CRVP is located, which can be seen from Fig. 18 and Fig. 20, and their legs do not extend all the way to the wake region. Likely, the origin of the upper hairpin structures is the instability of the jet trajectory.[32]

Fluid originating from off-center-plane of the jet follows lower trajectory and constitutes the wake of the jet, which extends about $1\,d$ in vertical and $2\,d$ in spanwise direction. Counter-rotating streamwise vorticity from the lateral boundaries of the jet is carried to the wake region and reorients in streamwise direction, creating strong counter-rotating vortex pair (CRVP), occupying the wake region and giving it elliptical cross-section. Lower hairpin vortex structures have their legs in the wake region. The legs are located at $z/d\ \pm 1$, which is also the position of the lateral boundaries of the wake region. It suggests that vertical vorticity of the legs is created by roll-up of streamwise CRVP tubes, occupying the lateral edges of the jet wake. Moreover, as the analysis of Fig. 22 shows, the instantaneous vertical vorticity in the wake region has a constant sign at the either side of the centerline $z/d = 0$, and this sign is consistent with CRVP rotation. Therefore, lower hairpin structures are possibly created by the CRVP instability mechanism proposed in Ref. 26. Top part of the lower hairpin structures should, therefore, have negative transverse vorticity. Looking at Fig. 13(a) one can notice the layer of negative vorticity at $2 < x/d < 3$, $2.5 < z/d < 3$, exactly where the upper parts of the lower structures should be. One can notice that lower hairpin structures are wider than the upper structures, having $2\,d$ versus $1.2\,d$ distance between its legs. Positive transverse vorticity in the center-plane at $1.6 < y/d < 2$ is brought from the windward side of the jet by the jet fluid which is carried around the jet and lifted up into the wake together with the crossflow fluid. Negative transverse vorticity next to the lee side of the jet occurs because of the deformation of the lee-side negative shear-layer vorticity.

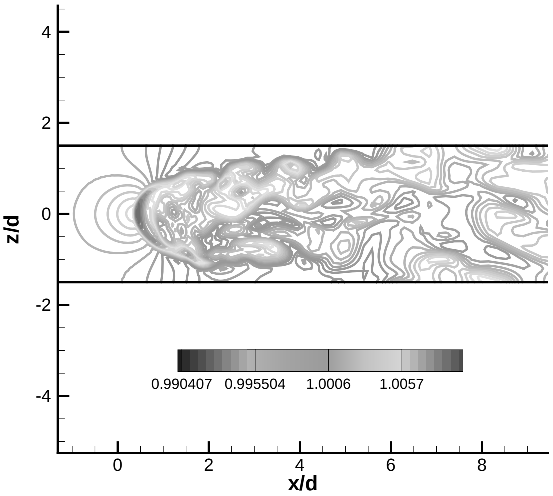

Figure 24. Contours of instantaneous temperature at $y/d \sim 1.75$.

V. Conclusions

Special parallel interface coupling compressible and low Mach number computational codes is developed in order to perform numerical investigations of film-cooling of turbine blades. The coupling procedure is tested on steady and unsteady laminar problems. Two types of tests are performed. First type of tests shows that in the low Mach number regime the difference between solutions obtained by two codes individually is very small. Second type of tests confirms that boundary conditions supplied from one code to another do not contaminate the solutions. Moreover, it is found that boundary conditions work even better in the presence of an auxiliary code than without it due to the larger amount of information available about the incoming or outgoing disturbances. Also, it is checked that the solution of the coupled problem does not drift from the solutions of individual codes.

This methodology is applied to the calculations of jet in a crossflow as a test problem for film-cooling applications. Laminar jet issuing into laminar crossflow with small velocity ratio characteristic of film-cooling flows is considered. The vortex systems of the jet-crossflow interaction are described and analyzed. Basic coherent structures characteristic of low velocity-ratio jets are identified in the present calculations. Analysis of three-dimensional streamlines suggests that the jet trajectory (streamline originating from the center of the jet exit) lies higher than the CRVP trajectory. Broad wake region of the jet is created by the fluid coming from the off-center-plane of the jet and from the windward side. CRVP occupies the wake region. Crossflow fluid goes around the jet and it is tackled into the wake region of the jet. Reverse flow zone exists behind the jet, no upright vortices of alternating vorticity sign are observed. Two layers of hairpin structures are revealed by looking at the positive isosurface of the Laplacian of pressure. Upper structures are linked to the jet shear-layer vortices and are probably generated by the instability of the jet trajectory proposed by Gamussi et al.[32] Lower structures appear in the wake region and have a vorticity sign consistent with CRVP. These structures might be generated by the elliptic instability of CRVP described by Blanchard et al.[26] Time-averaged streamline pattern compares well with the calculations of Muppidi et al.[33] Location of the node point shows good agreement with the value obtained by Muppidi et al. Hovering vortex at the left side of the jet is resolved by the low Mach number code, but not by the compressible code. This suggests that the resolution of the compressible code must be increased in the region of the jet issuance in order to capture the near wall structures.

VI. Acknowledgements

This work is supported by the Advanced Simulation and Computing (ASC) program of the Department of Energy. The compressible code was developed with AFOSR support under grant No. F94620-01-1-0138. The computer time is provided by the parallel DURIP-DARPA cluster of Stanford University.

References

[1] Burd, S. W., Kaszeta, R. W., and Simon, T. W., "Measurements in Film Cooling Flows: Hole L/D and Turbulence Intensity Effects," *Transactions of the ASME. The Journal of Turbomachinery*, Vol. 120, Oct. 1998, pp. 791–798.

[2] Burd, S. W. and Simon, T. W., "Turbulence Spectra and Length Scales Measured in Film Coolant Flows Emerging From Discrete Holes," *Transactions of the ASME. The Journal of Turbomachinery*, Vol. 121, July 1999, pp. 551–557.

[3] Ou, S., Mehendale, A. B., and Han, J. C., "Influence of High Mainstream Turbulence on Leading Edge Film Cooling Heat Transfer," *Transactions of the ASME. The Journal of Turbomachinery*, Vol. 114, Oct. 1992, pp. 707–733.

[4] Reiss, H. and Bölcs, A., "Experimental Study of Showerhead Cooling on a Cylinder Comparing Several Configurations Using Cylindrical and Shaped Holes," *Transactions of the ASME. The Journal of Turbomachinery*, Vol. 122, Jan. 2000, pp. 161–169.

[5] Mee, D. J., Ireland, P. T., and Bather, S., "Measurement of the Temperature Field Downstream of Simulated Leading-Edge Film-Cooling Holes," *Experiments in Fluids*, Vol. 27, 1999, pp. 273–283.

[6] Drost, U. and Bölcs, A., "Investigation of Detailed Film Cooling Effectiveness and Heat Transfer Distributions on a Gas Turbine Airfoil," *Transactions of the ASME. The Journal of Turbomachinery*, Vol. 121, April 1999, pp. 233–242.

[7] Polanka, M. D., Cutbirth, J. M., and Bogard, D. G., "Three Component Velocity Field Measurements in the Stagnation Region of a Film Cooled Turbine Vane," Tech. Rep. 2001–GT–0402, Proceedings of ASME TURBOEXPO, June 4-7, 2001, New Orleans, Louisiana, USA.

[8] Cutbirth, J. M. and Bogard, D. G., "Evaluation of Pressure Side Film Cooling with Flow and Thermal Field Measurements, Part I: Showerhead Effects," Tech. Rep. GT–2002–30174, Proceedings of ASME TURBOEXPO, June 3-6, 2002, Amsterdam, The Netherlands.

[9] Cutbirth, J. M. and Bogard, D. G., "Evaluation of Pressure Side Film Cooling with Flow and Thermal Field Measurements, Part II: Turbulence Effects," Tech. Rep. GT–2002–30175, Proceedings of ASME TURBOEXPO, June 3-6, 2002, Amsterdam, The Netherlands.

[10] Leylek, J. H. and Zerkle, R. D., "Discrete-Jet Film Cooling: A Comparison of Computational Results With Experiments," *Transactions of the ASME. The Journal of Turbomachinery*, Vol. 116, July 1994, pp. 358–368.

[11] Walters, D. K. and Leylek, J. H., "A Systematic Computational Methodology Applied to a Three-Dimensional Film-Cooling Flowfield," *Transactions of the ASME. The Journal of Turbomachinery*, Vol. 119, Oct. 1997, pp. 777–785.

[12] Walters, D. K. and Leylek, J. H., "A Detailed Analysis of Film-Cooling Physics: Part I - Streamwise Injection With Cylindrical Holes," *Transactions of the ASME. The Journal of Turbomachinery*, Vol. 122, Jan. 2000, pp. 102–112.

[13] Tyagi, M. and Acharya, S., "Large Eddy Simulation of Film Cooling Flow From an Inclined Cylindrical Jet," *Transactions of the ASME. The Journal of Turbomachinery*, Vol. 125, No. 4, Oct. 2003, pp. 734–742.

[14] Medic, G. and Durbin, P. A., "Toward Improved Film Cooling Prediction," *Transactions of the ASME. The Journal of Turbomachinery*, Vol. 124, April 2002, pp. 193–199.

[15] Bohn, D. E. and Kursterer, K. A., "Aerothermal Investigations of Mixing Flow Phenomena in Case of Radially Inclined Ejection Holes at the Leading Edge," *Transactions of the ASME. The Journal of Turbomachinery*, Vol. 122, April 2000, pp. 334–339.

[16] Xiong, Z. and Lele, S. K., "Numerical Study of Leading Edge Heat Transfer under Free-Stream Turbulence," AIAA Paper 2001–1016, Jan. 2001, In 39th AIAA Aerospace Sciences Meeting and Exhibit.

[17] Xiong, Z., "Stagnation Point Flow and Heat Transfer under Free-Stream Turbulence," Ph.d. thesis, Aug. 2004, Deparment of Mechanical Engineering, Stanford University.

[18] Pierce, C. D., "Progress-Variable Approach for Large Eddy Simulaiton of Turbulent Combustion," Ph.d. thesis, June 2001, Deparment of Mechanical Engineering, Stanford University.

[19] Harlow, F. H. and Welch, J. E., "Numerical Calculation of Time-Dependent Viscous Incompressible Flow," *Physics of Fluids*, Vol. 8, 1965, pp. 2182–2189.

[20] Leonard, B. P., "A Stable and Accurate Convective Modelling Procedure Based on Quadratic Upstream Interpolation," *Computational Methods in Applied Mechanics and Engineering*, Vol. 19, 1979, pp. 59–98.

[21] Germano, M., Piomelli, U., Moin, P., and Cabot, W. H., "A Dynamic Subgrid-scale Eddy Viscosity Model," *Physics of Fluids, A3*, 1991, pp. 1760–1765.

[22] Müller, B., "Low Mach Number Asymptotics of the Navier-Stokes Equations and Numerical Implicatons," *30th Computational Fluid Dynamics*, von Karman Institute for Fluid Dynamics, Lecture Series 1999–03, March 1999, pp. 821–831.

[23] Taylor, G. I., "On the Dissipation of Eddies," *Aero.Res.Comm, R and M*, 1918, pp. 598.

[24] Colonius, T., Lele, S. K., and Moin, P., "The Free Compressible Viscous Vortex," *Journal of Fluid Mechanics*, Vol. 230, 1991, pp. 45–73.

[25] Kelso, R. M., Lim, T. T., and Perry, A. E., "An Experimental Study of Round Jets in Cross-Flow," *Journal of Fluid Mechanics*, Vol. 306, 1996, pp. 111–144.

[26] Blanchard, J. N., Brunet, Y., and Merlen, A., "Influence of a Counter Rotating Vortex Pair on the Stability of a Jet in a Cross Flow: an Experimental Study by Flow Visualizations," *Experiments in Fluids*, Vol. 26, 1999, pp. 63–74.

[27] Fric, T. F. and Roshko, A., "Vortical Structure in the Wake of a Transverse Jet," *Journal of Fluid Mechanics*, Vol. 279, Nov. 1994, pp. 1–47.

[28] Hasselbrink, E. F. and Mungal, M. G., "Transverse Jets and Jet Flames," *Journal of Fluid Mechanics*, Vol. 443, 2001, pp. 1–68.

[29] Gopalan, R., Abraham, B. M., and Katz, J., "The Structure of a Jet in Cross Flow at Low Velocity Ratios," *Physics of Fluids*, Vol. 16, No. 6, June 2004, pp. 2067–2087.

[30] Peterson, S. D. and Plesniak, M. W., "Short-Hole Jet-in-Crossflow Velocity Field and its Relationship to Film-Cooling Performance," *Experiments in Fluids*, Vol. 33, Aug. 2002, pp. 889–898.

[31] Peterson, S. D. and Plesniak, M. W., "Evolution of Jets Emanating from Short Holes into Crossflow," *Journal of Fluid Mechanics*, Vol. 503, 2004, pp. 57–91.

[32] Gamussi, R., Guj, G., and Stella, A., "Experimental Study of a Jet in a Crossflow at Very Low Reynolds Number," *Journal of Fluid Mechanics*, Vol. 454, 2002, pp. 113–144.

[33] Muppidi, S. and Mahesh, K., "Study of Trajectories of Jets in Crossflow using Direct Numerical Simulations," *Journal of Fluid Mechanics, Accepted for publication*, 2005.